

Quantification of 3-D regional myocardial deformation: shape-based analysis of magnetic resonance images

ALBERT J. SINUSAS,^{1,2} XENOPHON PAPADEMETRIS,² R. TODD CONSTABLE,²
DONALD P. DIONE,¹ MARTIN D. SLADE,¹ PENGCHENG SHI,³ AND JAMES S. DUNCAN^{2,3}

¹Section of Cardiovascular Medicine, Department of Internal Medicine, ²Department of Diagnostic Radiology, and ³Department of Electrical Engineering, Yale University School of Medicine, New Haven, Connecticut 06520-8042

Received 24 January 2000; accepted in final form 11 March 2001

Sinusas, Albert J., Xenophon Papademetris, R. Todd Constable, Donald P. Dione, Martin D. Slade, Pengcheng Shi, and James S. Duncan. Quantification of 3-D regional myocardial deformation: shape-based analysis of magnetic resonance images. *Am J Physiol Heart Circ Physiol* 281: H698–H714, 2001.—A comprehensive three-dimensional (3-D) shape-based approach for quantification of regional myocardial deformations was evaluated in a canine model ($n = 8$ dogs) with the use of cine magnetic resonance imaging. The shape of the endocardial and epicardial surfaces was used to track the 3-D trajectories of a dense field of points over the cardiac cycle. The shape-based surface displacements are integrated with a continuum biomechanics model incorporating myofiber architecture to estimate both cardiac- and fiber-specific endocardial and epicardial strains and shears for 24 left ventricular regions. Whereas radial and circumferential end-systolic strains were fairly uniform, there was a significant apex-to-base gradient in longitudinal strain and radial-longitudinal shear. We also observed transmural epicardial-to-endocardial gradients in both cardiac- and fiber-specific strains. The increase in endocardial strain was accompanied by increases in radial-longitudinal shear and radial-fiber shears in the endocardium, supporting previous theories of regional myocardial deformation that predict considerable sliding between myocardial fibers.

myocardial strain; finite element analysis; fiber architecture; cardiac mechanics

THE HEART UNDERGOES A COMPLEX three-dimensional (3-D) deformation with each cardiac cycle. Regional myocardial deformation (strain) is determined by several factors, including local material properties, local contractile function, and global forces such as left ventricular pressure. Many approaches (3, 5, 14, 36, 42–45) have been employed to evaluate the complex cyclic regional deformations of the heart. Most studies that have attempted to analyze the detailed deformations of the heart have employed methodology that permits analysis of only a very limited area of the myocardium. These approaches are highly invasive and involve implantation of arrays of either radio-opaque beads or sonomicrometers in the myocardium (9, 14, 15, 22, 29,

42–44). In the analysis of implanted radio-opaque beads, deformations are defined by analysis of the 3-D displacement of the beads by using biplane cine angiography. This approach offers reasonable spatial and temporal resolution, although it is quite tedious and can be confounded by errors associated with localization of the beads in 3-D space (14, 29). The sonomicrometry approach offers both higher spatial and temporal resolution but is also highly invasive (10, 15, 27, 36). In both approaches, implantation of the beads or sonomicrometers may themselves alter the pattern of regional deformation (14).

The development of magnetic resonance (MR) imaging tagging has enabled a more comprehensive noninvasive analysis of the complex deformations of the heart (2, 5, 45). This approach requires specific imaging sequences, which impart signal voids in the myocardium that are tracked over time. This approach generally provides analysis of regional deformation in fixed imaging planes. A few studies (5, 6) have attempted to derive 3-D deformations by integrating orthogonal image sets. These analyses demonstrated that deformation of the left ventricle is not uniform.

We have developed a comprehensive 3-D shape-based approach for quantification of regional myocardial deformations that can be applied to any high-resolution cine 3-D image set (11–13, 26, 33, 39). Local shape properties of the endocardial and epicardial surfaces are used to derive 3-D trajectories for a dense field of points over the entire cardiac cycle. These trajectories are then used to deform a mesh that represents the left ventricular myocardial volume. This analysis is embedded in a unifying framework by using a continuum biomechanics model. The resulting equations are solved with the use of the finite-element method. This shape-based approach for tracking regional myocardial deformation has been (39) validated in both 2- and 3-D, by comparing algorithm-derived trajectories with displacements derived with the use of implanted endocardial and epicardial markers. Recently, Papademetris (30) extended this validation for

Address for reprint requests and other correspondence: A. J. Sinusas, Yale Univ. School of Medicine, P.O. Box 208017, 3FMP, New Haven, CT 06520-8017 (E-mail: albert.sinusas@yale.edu).

The costs of publication of this article were defrayed in part by the payment of page charges. The article must therefore be hereby marked “advertisement” in accordance with 18 U.S.C. Section 1734 solely to indicate this fact.

determination of regional myocardial strain by using the same implanted marker system.

We now extend this shape-based analysis of MR-derived displacements to compute regional cardiac- and fiber-specific strains and shears over the cardiac cycle for all regions of the left ventricle. In this study, we use shape-based surface displacements together with a continuum biomechanics model incorporating myofiber architecture to estimate endocardial and epicardial fiber-specific strains. The normal pattern of myocardial deformation was studied by using our shape-based approach in closed-chest dogs. Whereas circumferential and radial strains were fairly uniform, there was a significant apex-to-base gradient in longitudinal strain and radial-longitudinal shear. We also observed transmural epicardial-to-endocardial gradients in both cardiac- and fiber-specific strains. The increase in endocardial strains was accompanied by increases in radial-longitudinal shear and radial-fiber shears in the endocardium. Transmural gradients in cardiac- and fiber-specific strains and shears support previous theories of regional myocardial deformation, which predict considerable sliding between myocardial fibers (9).

METHODS

Experiments were performed on fasting adult mongrel dogs with approval of the Yale Animal Care and Use Committee and in compliance with the guiding principles of the American Physiological Society on research animal use. All dogs were anesthetized intravenously with 10–12 mg/kg of thiopental sodium (Pentothal, Abbott; Chicago, IL), intubated, and mechanically ventilated on a respirator with a mixture of halothane (0.5%–1.5%) and N₂O and O₂ (3:1). Arterial pH, PCO₂, and PO₂ were measured serially, and the ventilator was adjusted to maintain these parameters within the physiological range. An electrocardiographic lead was monitored continuously.

Surgical Preparation/Experimental Protocol

A femoral vein and both femoral arteries were isolated and cannulated for administration of fluids and drugs, pressure monitoring, and arterial sampling. A thoracotomy was performed in the fifth intercostal space. An incision was made in the pericardium, and the proximal left anterior descending coronary artery was isolated for placement of a snare occluder. This occluder was externalized and the chest was closed in layers.

After surgical preparation was completed, the dogs were positioned in the MR scanner for imaging. An electrocardiographic limb lead was monitored continuously during MR imaging and used for gating. Resting MR images were completed in 1 h. Heart rate (HR) and aortic pressure (AoP) were recorded immediately before and after each complete image acquisition. Dogs subsequently underwent repeat MR imaging after coronary occlusion as part of a separate investigation. Dogs were euthanized with a bolus of potassium chloride after completing all imaging.

MR Image Acquisition

MR imaging was performed on a GE Signa 1.5 T scanner with version 4.8 GE software by using the head coil (26-cm

diameter) for transmission and reception. Short-axis images through the left ventricle were obtained with the gradient echo cine technique by using the following parameters: echo time = 6 ms, repetition time = 40 ms, flip angle = 30°, 16 phases collected, 5-mm slices, matrix 256 × 256, two averages, and field of view = 40 cm. A total of 16 contiguous 5-mm-thick slices were collected by acquiring four sets of staggered short-axis slices (4 slices/set) with a separation gap of 20 mm and 5 mm offset. This sequence provides images with an in plane resolution of 1.64 × 1.64 mm for a 256 × 256 matrix and a 5-mm resolution perpendicular to the imaging plane. This sequence also provides excellent temporal resolution (16 frames/cardiac cycle, ≈40 ms/frame).

Image Analysis

All image analysis was completed off-line after the completion of each study with the use of a Silicon Graphics workstation (Octane, R10000, 195 MHz, 128 MB RAM).

Visually interactive semiautomated 3-D segmentation of MR images. A semiautomated technique for left ventricular endocardial and epicardial boundary segmentation was utilized to improve reproducibility of surface contour generation. A software package was developed at Yale University specifically for this purpose on the Silicon Graphics platform (31). The package has an intuitive user interface and can simultaneously display orthogonal views of the 3-D image and multiple surface sections as well as multiple 3-D surface renderings from any angle. All components of the display can also be shown in cine mode. The colors and transparency of the surfaces can be edited to allow the user to display one surface inside another. After the contours in an initial slice are defined, the algorithm automatically propagates contours to adjacent slices. Defined contours are used as an initialization for the subsequent or preceding time frames, and therefore contours are also propagated through each time frame (7, 8). All contours were reviewed by superimposing them on the corresponding image slices, and, if necessary, corrected by using simple manual point and click operations within the platform. Contours are then assembled into complete endocardial and epicardial surfaces within this platform (31) by using Delaunay triangulation.

Shape-based displacement computation. Once the surfaces are extracted, we compute the principal curvatures for local regions on each surface at each time point. The initial frame-to-frame correspondences are then established between points on the surfaces by using a shape-tracking approach. For each point on a surface in the initial time frame, a search window is generated on the associated surface of the next time frame containing all plausible candidate corresponding points. We define the corresponding point as the point in the search window that has the closest shape properties to the original point. The shape properties are defined by using the curvatures of local surface regions (see APPENDIX). The strength and uniqueness of each local match was preserved as a confidence measure for the match (38). Regional endocardial and epicardial displacements were computed by using this previously described shape-based surface tracking approach for surfaces derived from two temporally successive images (12). We have previously validated this approach for tracking points on the surface of the heart by comparing shape-derived trajectories with displacements derived from endocardial and epicardial surface markers (39).

Deformation modeling and analysis. We have developed a framework from which we can compute myocardial deformation by integrating shape-tracked surface displacement data

with knowledge about the mechanical properties of the tissue. The details of this approach were summarized in a previous publication (32) and outlined in the APPENDIX. We model the imaged 3-D section of the myocardium as a transversely isotropic elastic solid continuum with preferential stiffness along fiber directions as defined by Guccione and McCulloch (19). This approach results in a set of partial differential equations, which provide relations between the displacements throughout the left ventricle. These equations are solved with the use of the finite-element method (21). The first step in this method is to divide the continuous structure of the object into finite pieces or elements to construct a finite element mesh. The equations are assembled in matrix form as $\mathbf{KU} = \mathbf{A}(\mathbf{U}^e - \mathbf{U})$, where \mathbf{K} is the stiffness matrix representing the material properties of the tissue, \mathbf{A} is loading matrix representing the confidence in the original shape-tracking-derived nodal displacements \mathbf{U}^e (where available), and \mathbf{U} is the nodal displacement vector field, which we are trying to estimate. This equation is solved to find the displacement field \mathbf{U} , which can then be differentiated to compute strain.

Strain analysis. In the finite-element discretization, the displacement field in each element is described by $\mathbf{u} = [\mathbf{N}][\mathbf{u}]$, where $[\mathbf{N}]$ is the interpolation matrix and $[\mathbf{u}]$ is the vector of displacements at the nodes. The strain ϵ is computed as $\epsilon = [\mathbf{B}][\mathbf{u}]$, where $[\mathbf{B}]$ is the strain to displacement Jacobian matrix. This produces strains in the global coordinate space. Strains were computed for each image frame relative to end diastole. The strains can be subsequently rotated to either a fiber-specific or a cardiac-specific coordinate system by using an appropriate rotation matrix.

Methods of Analysis

Application of our shape-based algorithm with finite element analysis and continuum mechanics provided an estimate of systolic and diastolic strains and shears for multiple small regions of the left ventricle. For purposes of describing the normal pattern of left ventricular deformation, the left ventricle was divided into three major short-axis slices (apical, midventricular, and basal), excluding the true apex and the base of the left ventricle at the membranous septum. Each slice was then divided into 8 circumferential wedges, resulting in 24 myocardial segments. Regional systolic myocardial strains were obtained for each of 24 "pie-shaped" myocardial segments. These transmural sections were then further divided into endocardial and epicardial segments. The end-systolic frame was determined for each dog by selecting the 3-D image frame with the smallest global left ventricular volume. Principal strains were computed for each image frame within the systolic period relative to the end-diastolic reference frame. Regional strains and shears were then derived with the use of two different axis systems. Strains were first generated with the use of a standard cardiac-specific axis, whereby the orthogonal strains were radial, circumferential, and longitudinal. The following cardiac-specific shears were also computed: radial-circumferential, radial-longitudinal, and circumferential-longitudinal. Strains were also rotated to fiber-specific axes previously described by Guccione and McCulloch (19) derived from histological studies by Streeter et al. (40), whereby the orthogonal strains and shears were cross-fiber strain, radial strain, fiber strain, cross-fiber-radial shear, cross-fiber-fiber shear, and radial-fiber shear. Regional myocardial strain data derived by using the two different coordinate systems were analyzed separately.

Statistical Analysis

By using the univariate procedure in Statistical Analysis Systems, it was determined that utilizing a normal approximation for the distributions of strain was appropriate. Analyses of variance (ANOVA) were performed to determine if there were significant differences in strain between the apical region, the midventricular region, and the basal region of the heart. ANOVA were also performed to determine if there were significant differences in strain between the eight circumferential regions of the heart (across the entire heart) as well as for each of the three slices separately. For all of these analyses, Tukey's test (honestly significant difference test) was performed on all main-effects means to determine significant differences. In comparison of endocardial and epicardial differences, paired Student's *t*-tests were performed on average values for each dog. All data are presented as means \pm SD. A level of significance, $\alpha = 0.05$, was utilized for all of the analyses performed.

RESULTS

Eight dogs completed the MR imaging protocol. Hemodynamic parameters and cardiac rhythm remained stable during the MR image acquisition. The HR and systolic AoP immediately before the MR acquisition (HR, 93 ± 22 beats/min; AoP, 108 ± 14 mmHg) were not significantly different from that obtained at the completion of the acquisition (HR, 94 ± 25 beats/min; AoP, 107 ± 20 mmHg). All image analyses were performed on all dogs.

3-D Maps of Cardiac- and Fiber-Specific Strain and Shear

Regional differences in myocardial systolic strains and shears were observed in normal hearts and are summarized below. An example of typical cardiac- and fiber-specific strain and shear patterns are shown for short-axis cutaway cross sections (see Fig. 1) at several different times points during the systolic interval. All six strain-tensor components were computed for both cardiac- and fiber-specific axes. The radial strain is common to both axes systems. The volume of the left ventricle can be cut and viewed along any axis to visualize the entire transmural strain pattern.

Analysis of Transmural Strain and Shear

Cardiac-specific strains and shears. Figure 2 illustrates the average regional transmural end-systolic cardiac-specific strains (Fig. 2A) and shears (Fig. 2B), which were computed for each of the 24 myocardial segments (3 slices and 8 radial sectors per slice). Radial (0.21 ± 0.03) and circumferential (-0.10 ± 0.01) strains were fairly uniform over the left ventricle. A significant ($P = 0.0001$) apex-to-base gradient in transmural longitudinal strain was observed (apical, 0.02 ± 0.02 ; midventricle, -0.01 ± 0.01 ; and basal, -0.03 ± 0.01). Apical segments tended to lengthen along the long axis of the heart, whereas basal segments demonstrated longitudinal shortening.

Transmural end-systolic cardiac-specific shears were less uniform. Small differences in radial-longitudinal and circumferential-longitudinal shears were seen at

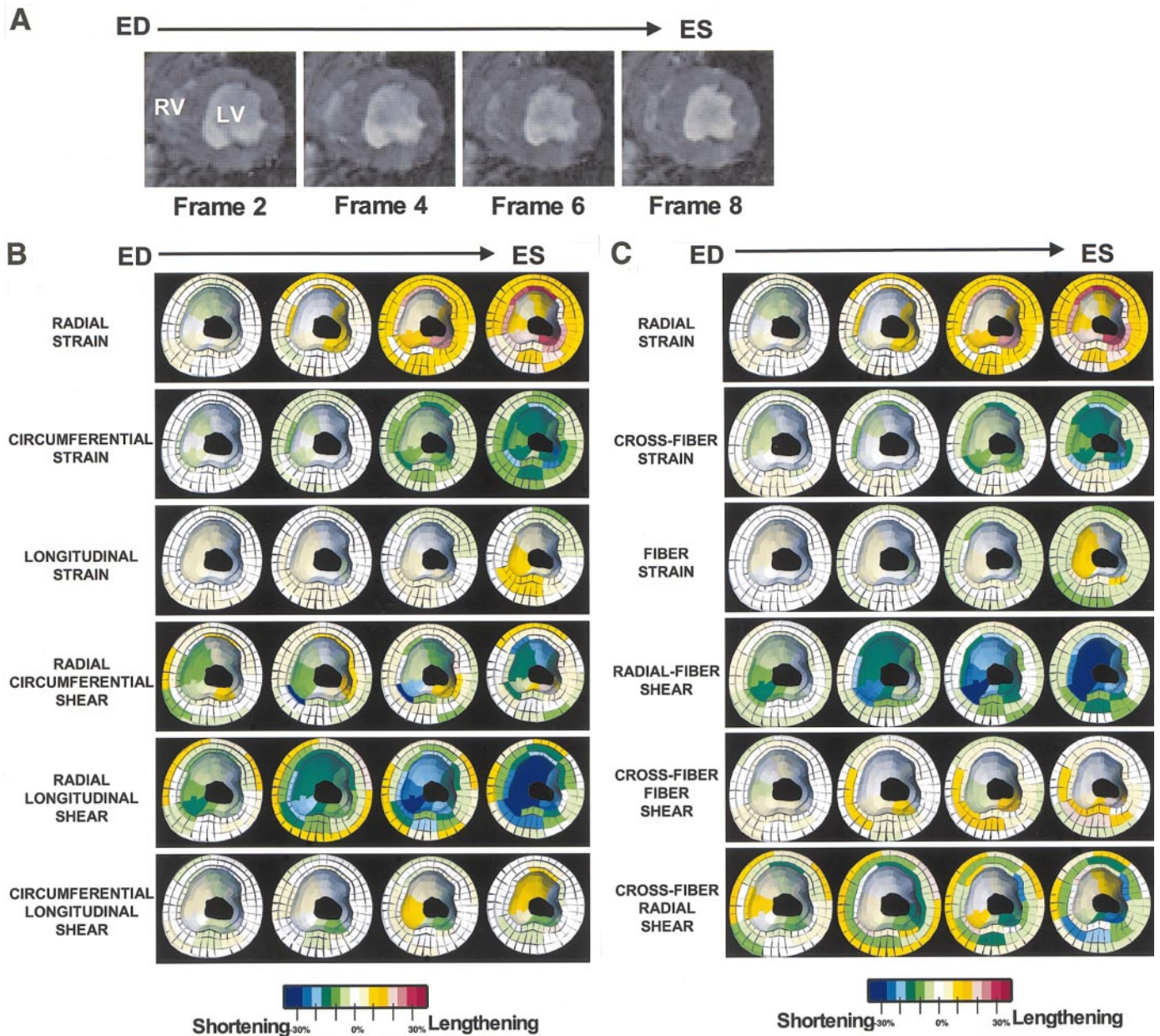
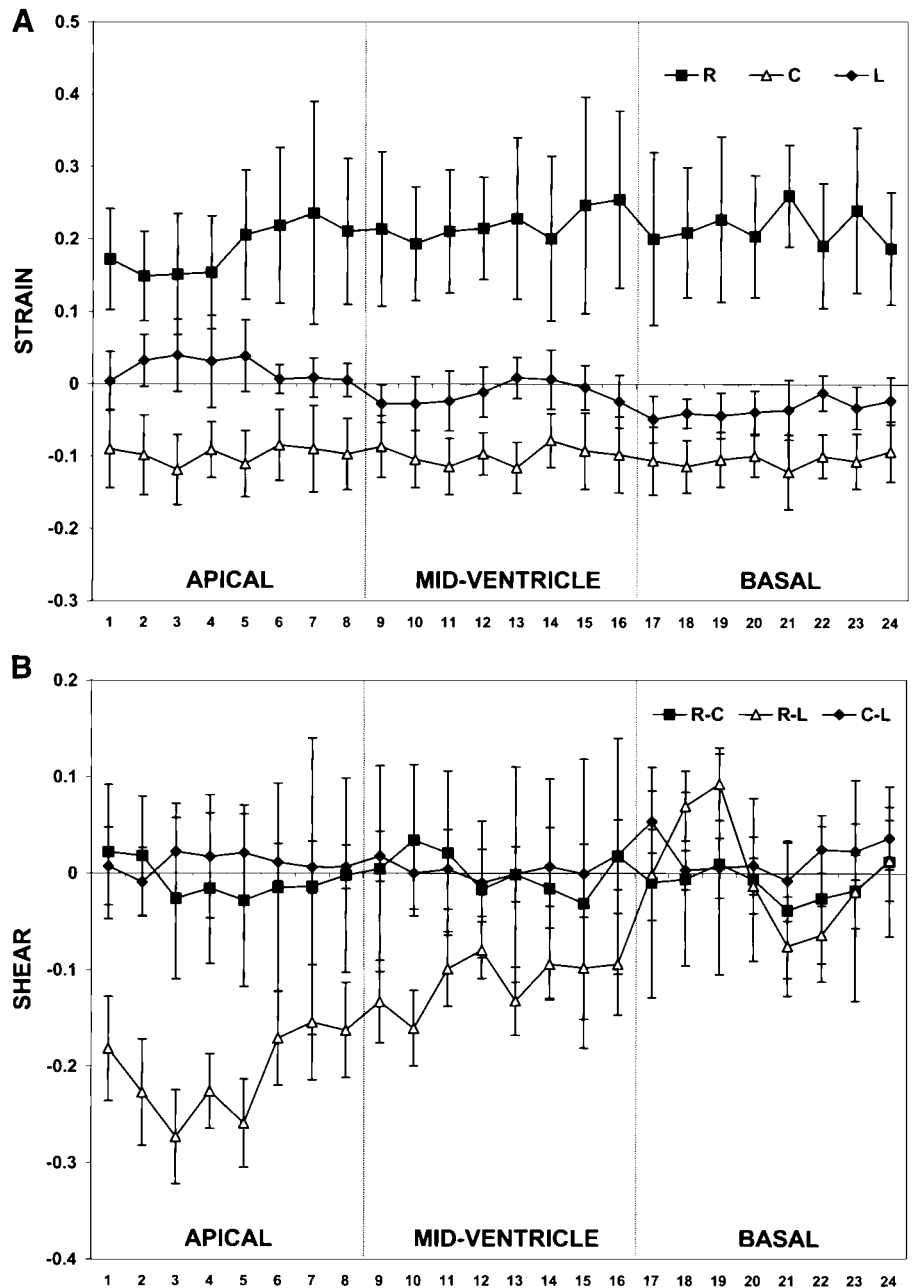


Fig. 1. Series of magnetic resonance (MR) short-axis systolic images (A) and corresponding short-axis cutaway color-coded maps of regional myocardial cardiac-specific (B) and fiber-specific (C) strains and shears from end diastole (ED) to end systole (ES) in a normal dog derived using the shape-based approach. Images are oriented with the right ventricle (RV) on left and the left ventricle (LV) on right. *Top*, anterior wall of the LV. *Bottom*, color code for the strain values. Blue and green color tones represent shortening, whereas red and yellow tones represent lengthening. All of the finite elements are shown in this cutaway view, although color-coded values are displayed for each of the 8 radial sectors. Note that strains and shears increase over the systolic interval. Radial and circumferential strains were greater in the subendocardium. Longitudinal strains were generally small. Among the cardiac-specific shears, the radial-longitudinal shears were the largest. Fiber strain was fairly uniform across the wall, whereas cross-fiber strain was greater in the subendocardium. Among the fiber-specific shears, radial-fiber and radial-cross-fiber shears were both large.

the base of the heart at the anterior and posterior junctions of the right and left ventricle. A more dramatic apex-to-base gradient of radial-longitudinal shear was observed (apical, -0.21 ± 0.05 ; midventricle, -0.11 ± 0.03 ; and basal, 0.001 ± 0.06 ; $P = 0.0001$). There appeared to be a hinge point in the basal septum in the region of the membranous septum.

Fiber-specific strains and shears. Figure 3 illustrates the average variation in regional transmural end-systolic fiber-specific strains (Fig. 3A) and shears (Fig. 3B). Fiber (-0.05 ± 0.01) and cross-fiber (-0.06 ± 0.02) strains were similar in magnitude and also fairly uniform around the left ventricle. There were small but significant apex-to-base differences in both fiber (api-

Fig. 2. Average regional transmural ES cardiac-specific strains (A) and shears (B), which were computed for each of the 24 myocardial segments (3 slices, 8 radial sectors per slice). Average regional values (means \pm SD) are shown. Radial (R) and circumferential (C) strains were fairly uniform throughout the heart. A significant ($P = 0.0001$) apex-to-base gradient in transmural longitudinal (L) strain was observed. Apical segments tended to lengthen along the long axis of the heart, whereas basal segments demonstrated longitudinal shortening. Small differences in R-L and C-L shears were seen at the base of the heart at the anterior and posterior junctions of the right and left ventricle. A more dramatic apex-to-base gradient of R-L shear was observed.



cal, -0.04 ± 0.01 ; midventricle, -0.05 ± 0.01 ; and basal, -0.06 ± 0.01 ; $P = 0.002$) and cross-fiber strain (apical, -0.04 ± 0.01 ; midventricle, -0.06 ± 0.01 ; and basal, -0.08 ± 0.01 ; $P = 0.0001$).

Significant differences in cross-fiber-radial and fiber-radial shear were seen at the base of the heart, again at the anterior and posterior junctions of the right and left ventricle. Significant apex-to-base gradients in both cross-fiber-radial (apical, -0.17 ± 0.02 ; midventricle, -0.07 ± 0.03 ; and basal, 0.02 ± 0.05 ; $P = 0.0001$) and fiber-radial (apical, -0.07 ± 0.03 ; midventricle, -0.06 ± 0.02 ; and basal, -0.03 ± 0.04 ; $P = 0.0005$) shears were also observed.

Analysis of Endocardial and Epicardial Strain and Shear

Average endocardial and epicardial cardiac-specific and fiber-specific strains and shears were computed for each dog for all of the predefined 24 left ventricular segments. Overall average endocardial and epicardial strain tensors were computed from the dog averages.

Cardiac-specific endocardial and epicardial strains and shears. Figure 4 provides a summary of the overall endocardial and epicardial cardiac-specific strains and shears. There were significant endocardial-epicardial

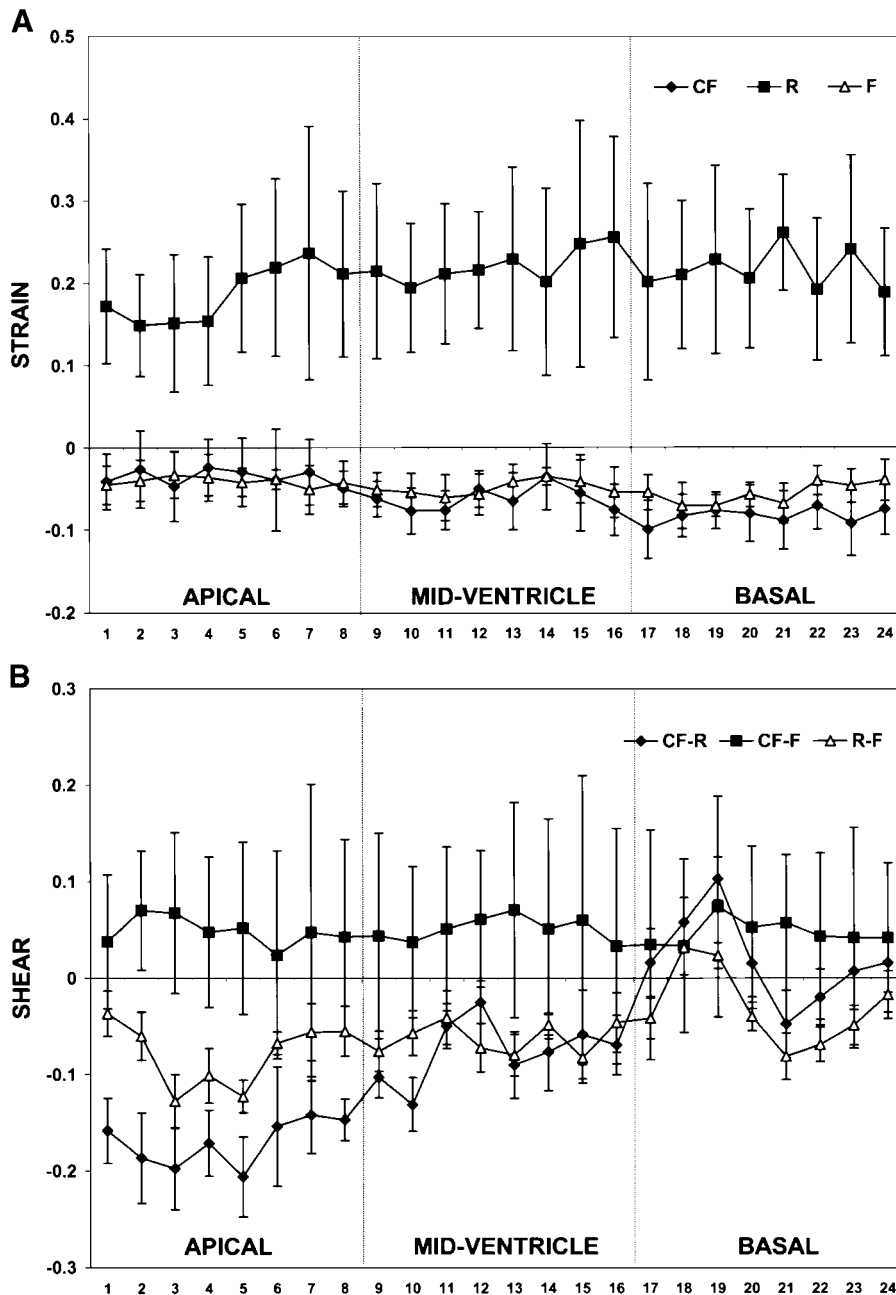


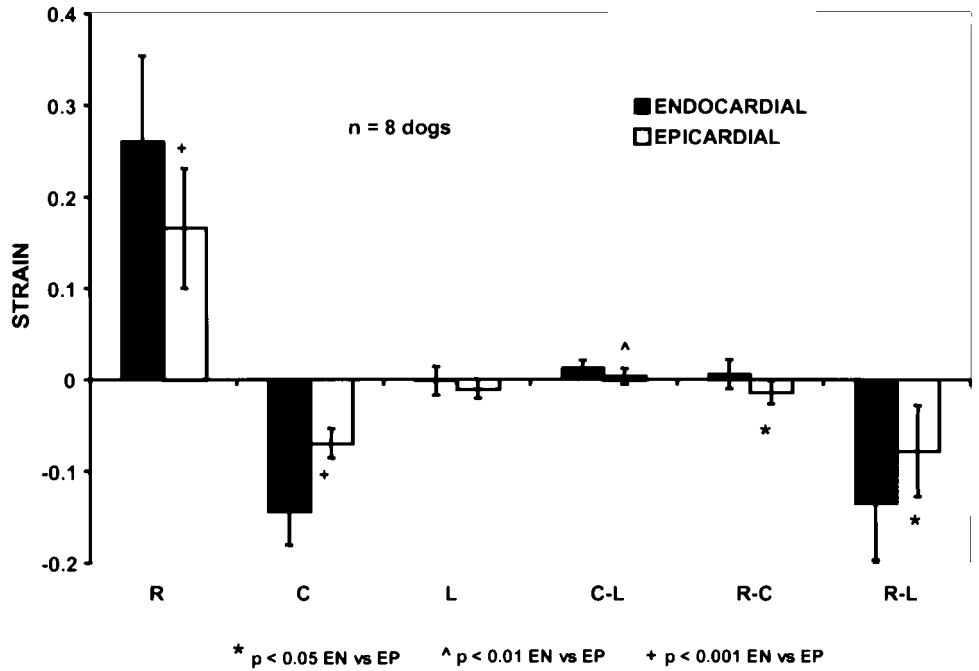
Fig. 3. Average regional transmural ES fiber-specific strains (A) and shears (B), which were computed for the same 24 myocardial segments as in Fig. 2. Fiber (F) and cross-fiber (CF) strain were similar in magnitude and also fairly uniform around the left ventricle. There were small but significant apex-to-base differences in both F and C-F strain. Significant differences in CF-R and R-F shear were seen at the base of the heart. Significant apex-to-base gradients in both CF-R and R-F shear were also observed.

gradients in both radial (endocardial, 0.26 ± 0.09 ; epicardial, 0.17 ± 0.07 ; $P = 0.0009$) and circumferential (endocardial, -0.14 ± 0.04 ; epicardial, -0.07 ± 0.02 ; $P = 0.0002$) strains. As previously described with the use of a variety of techniques, greater radial and circumferential strain occurred in the subendocardial region. These differences in strains between the endocardial and epicardial segments were associated with small but significant differences in all three shears.

Fiber-specific endocardial and epicardial strains and shears. Figure 5 summarizes of the endocardial and epicardial fiber-specific strains and shears. There was slightly greater strain along the fiber

direction in the epicardium. However, a prominent endocardial-epicardial gradient in cross-fiber strain was observed (endocardial, -0.11 ± 0.03 ; epicardial, -0.02 ± 0.01 ; $P = 0.0001$). This increase in endocardial cross-fiber strain was associated with large fiber-cross-fiber (endocardial, 0.09 ± 0.02 ; epicardial, 0.01 ± 0.01 ; $P = 0.00002$) and radial-fiber (endocardial, -0.10 ± 0.05 ; epicardial, -0.03 ± 0.02 ; $P = 0.0002$) shears, suggesting that much of the deformation in the endocardium can be attributed to cross-fiber sliding or changes in fiber separation. The increase in endocardial deformation with respect to the epicardium does not appear to be attributable to increases in endocardial fiber shortening.

Fig. 4. Average endocardial and epicardial cardiac-specific strains and shears. Both R and C strains were greater in the endocardium than the epicardium. L strains were uniform across the wall. There was a significant endocardial-to-epicardial gradient in all three cardiac-specific shears (C-L, R-C, and R-L). The largest shear occurred in the transverse (R-L) direction.



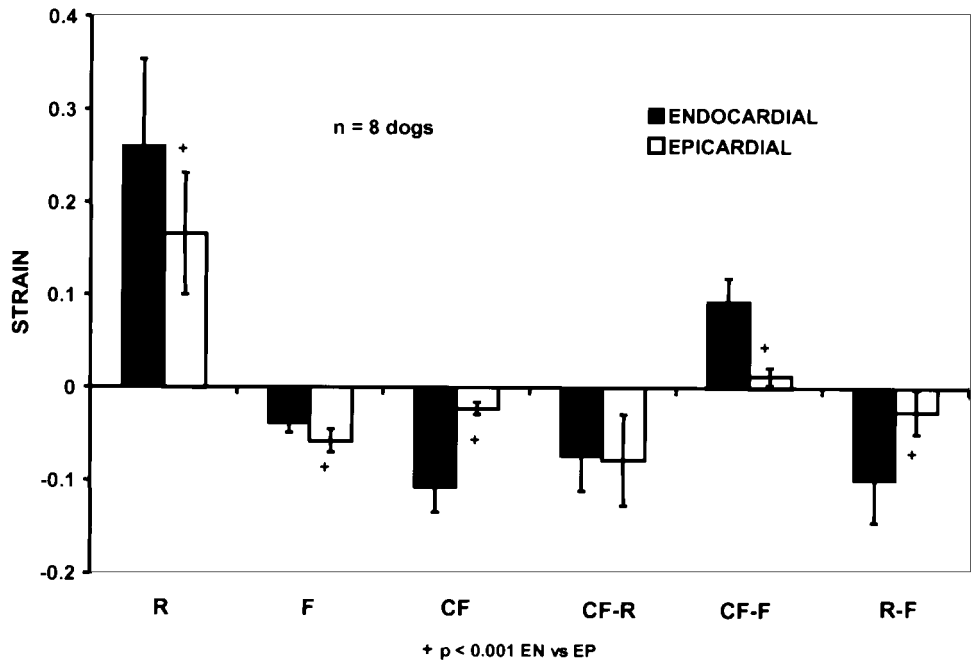
Temporal Changes in Systolic Strains

The proposed approach for analysis of regional myocardial deformation can also provide temporal changes in endocardial and epicardial systolic strain and shear. An example of the temporal changes in systolic cardiac- and fiber-specific strains is shown in Fig. 6. The observed endocardial-epicardial gradients in radial, circumferential, and cross-fiber strains were generally preserved for all 24 myocardial regions throughout the systolic interval.

Temporal Changes in Average Systolic and Diastolic Strains

Our approach can also provide information regarding diastolic strain. An example of the temporal changes in average cardiac- and fiber-specific strain over the entire cardiac cycle is shown for a representative dog (Fig. 7). Diastolic strain could not be derived for all of the dogs in this series of experiments because of image flow artifacts at the endocardial surface of the heart during the diastolic pe-

Fig. 5. Average endocardial and epicardial fiber-specific strains and shears. Both F and CF strains were significantly greater in the endocardium than the epicardium, although the magnitude of the CF strain was larger. There was a significant endocardial-to-epicardial gradient in all CF-F and R-F shears. There was no gradient in CF-R shear.



riod complicating surface segmentation. The strains and shears generally returned to baseline at end diastole with an appropriate leveling off in late diastole. The failure of average longitudinal strains to return to baseline during diastole reflects regional variation in longitudinal strain, particularly in basal segments.

DISCUSSION

We employed a novel 3-D shape-based analysis of standard cine MR cardiac images for the comprehensive assessment of regional left ventricular deformation. The normal regional patterns of transmural left ventricular systolic cardiac- and fiber-specific deformations were defined in an experimental canine model. Regional endocardial and epicardial strains were also computed noninvasively and are consistent with measures previously derived by using highly invasive methodology. These object-centered parameters of deformation have a clear advantage over frame-centered parameters like displacements and velocities, because regional myocardial strain is independent of translational and rotational motion of the heart. Transmural myocardial radial and circumferential strains were fairly uniform throughout the left ventricle. Significant apex-to-base gradients were observed for longitudinal strain and several of the shear strains, in particular radial-longitudinal (transverse) shear. An epicardial-to-endocardial gradient in radial and circumferential strain was observed throughout the left ventricle. There was also an increase in cross-fiber strain in the endocardium. An increase in endocardial strains was accompanied by increases in radial-longitudinal and radial-fiber shears in the endocardium. Thus the transmural gradients in cardiac- and fiber-specific strains and shears support previous theories of regional myocardial deformation, which predict considerable sliding between myocardial fibers.

Quantitative Analysis of Left Ventricular Deformation

The left ventricle is a 3-D object that moves linearly and nonlinearly in space over the cardiac cycle. The myocardium is also a complex 3-D structure consisting of myocytes interconnected by a dense collagen weave that course in different directions. Under normal conditions, the myocardium undergoes a complex cyclic deformation. We can expect that regional ischemia and infarction will produce even more complex changes in regional and global deformation. Ideally, one would like to track these changes in regional deformation in a 3-D space.

Most standard approaches for regional analysis of function have focused on the measurement of endocardial motion or left ventricular thickening from two-dimensional (2-D) image sequences. Some of these approaches have relied on volumetric information, such as regional ejection fractions, derived from radial segments extending from the center of the ventricle. This approach is dependent on the

reproducible location of references from which to make regional measurements. To alleviate the problems associated with reliably marking reference points on the left ventricle, the reference-free centerline method was developed (37). However, the centerline approach can only compute changes in deformation along the radial direction and does not account for potential deformations out of the imaging plane (20).

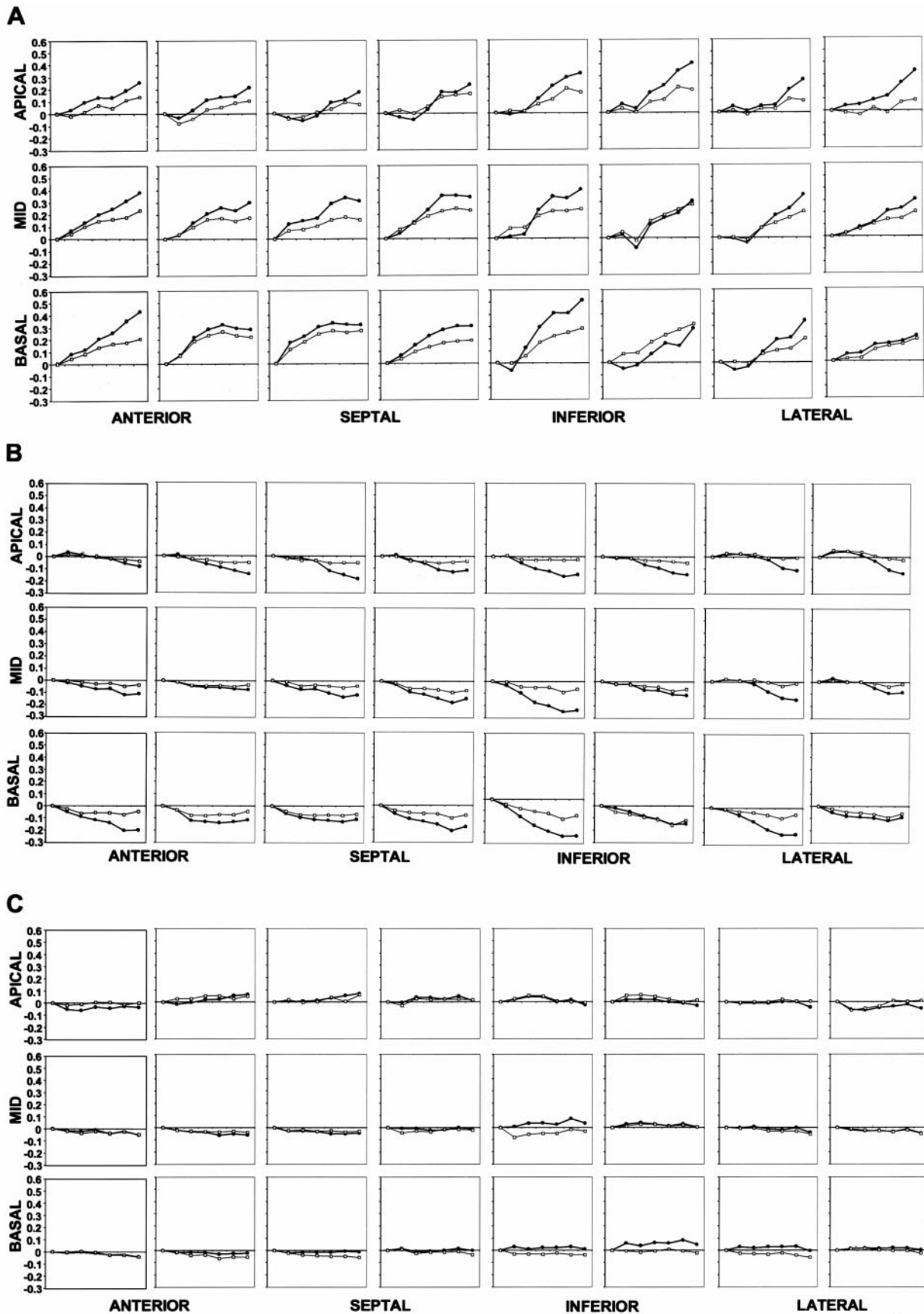
Invasive Measurements of Regional 3-D Deformation and Strain

Much of the information gained regarding 3-D deformation of the left ventricle comes from analysis of implanted radio-opaque markers that use biplane cine radiography. Whereas this approach has certain merits, there are also significant limitations. One obvious concern is the effect of bead implantation. Fenton et al. (14) reported an average flow decrease of 25% within 5 mm of marker implantation. Additionally, there are errors associated with localization of the markers in a 3-D space (± 0.15 – 0.2 mm) (14, 29). This error is due to the pincushion effect, cone effect, and identification of the marker centroids, which is in part dependent on the marker size.

Other investigators have computed regional strains with implanted sonomicrometers. This approach offers greater temporal (sampling rate 120–150 Hz) and spatial resolution (27). The higher spatial resolution of the crystals may permit an equally accurate determination of transmural strain with smaller sized and fewer numbers of implanted crystals. However, analysis with this approach is also limited to a finite region of the left ventricle. Again, implantation of the crystals, like implantation of the beads, may alter regional deformation and flow.

Analysis of 3-D Deformation

Many studies evaluating 3-D deformation in the heart assume that myocardial deformation is homogeneous. An important finding of some earlier studies is that systolic myocardial deformation is indeed not homogeneous. Significant transmural gradients of strain have been observed. Continuous transmural strain distributions can be obtained from the nonhomogeneous model, as proposed by McCulloch and Omens (24). This model computes continuous transmural variations in strain and rotation by using 3-D nonlinear finite element interpolating functions for nonhomogeneous deformation analysis (24). To date, only a few recent studies (29) have incorporated this more sophisticated analysis of myocardial deformation because of the time intensive computations required. We employ a 3-D shape-based approach for analysis of cine MR images, which integrates image-derived shape-tracked surface displacement data and fiber orientation data with a transversely isotropic elastic solid continuum model with preferential stiffness along fiber directions.



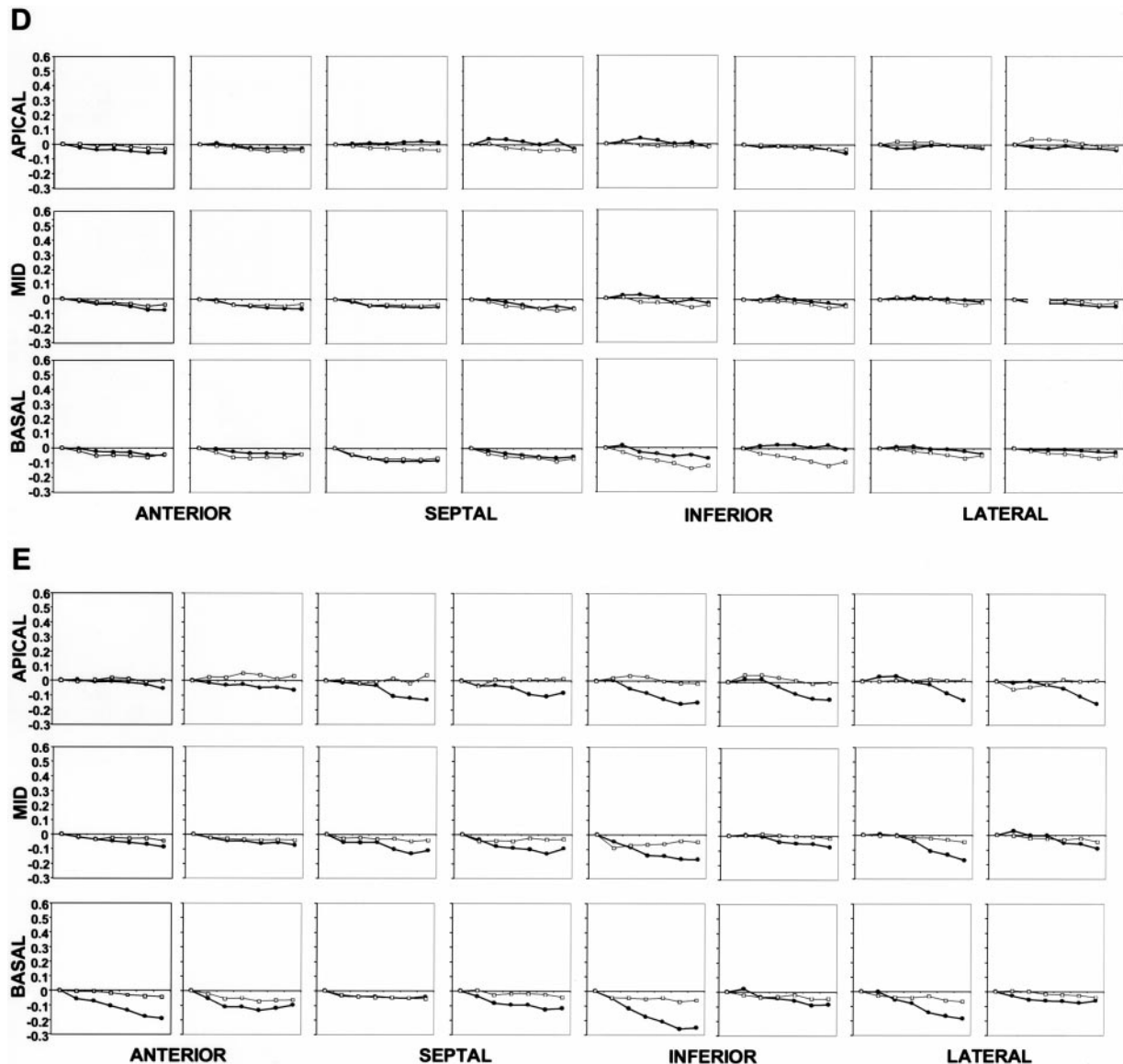


Fig. 6. Example of temporal changes in systolic cardiac- and fiber-specific strains from a representative dog for both endocardial (●) and epicardial (□) segments. Shown are R (A), C (B), L (C), F (D), and C-F (E) systolic strains for 8 radial segments for three short-axis sections: apical, mid (midventricular), and basal. The observed endocardial-epicardial gradients in R, C, and CF strains were generally preserved for the 24 myocardial regions throughout the systolic interval.

Calculation of Cardiac-Specific Strains and Shears

The cardiac-specific strains and shears derived using our 3-D image-based approach are similar to those previously derived in the dog by using more invasive approaches. Villarreal et al. (42) evaluated regional myocardial deformation in dogs with the use of biplane radiography of implanted transmural arrays of radioopaque beads (as described above). Cardiac-specific strains were computed for subepicardial, midwall, and subendocardial regions. These investigators demonstrated systolic radial strain (ϵ_{rr}) was positive under control conditions. In contrast, circumferential (ϵ_{cc}) and longitudinal (ϵ_{ll}) systolic strains were negative. They also observed small positive systolic transverse

shear deformations [circumferential-radial (ϵ_{cr}), 0.05; and longitudinal-radial (ϵ_{lr}), 0.08] under control conditions. During control conditions, these investigators identified the usual epicardial to endocardial gradient in both circumferential and radial strains, with the greatest deformations occurring in the endocardial region. An earlier publication by Fenton et al. (14), using a similar implanted bead methodology, also demonstrated different patterns of deformation in endocardial regions relative to epicardial and midwall regions. The endocardial deformation was complex and also had large transverse shear components under control conditions.

The cardiac-specific strains and shears determined by using our comprehensive noninvasive shape-based

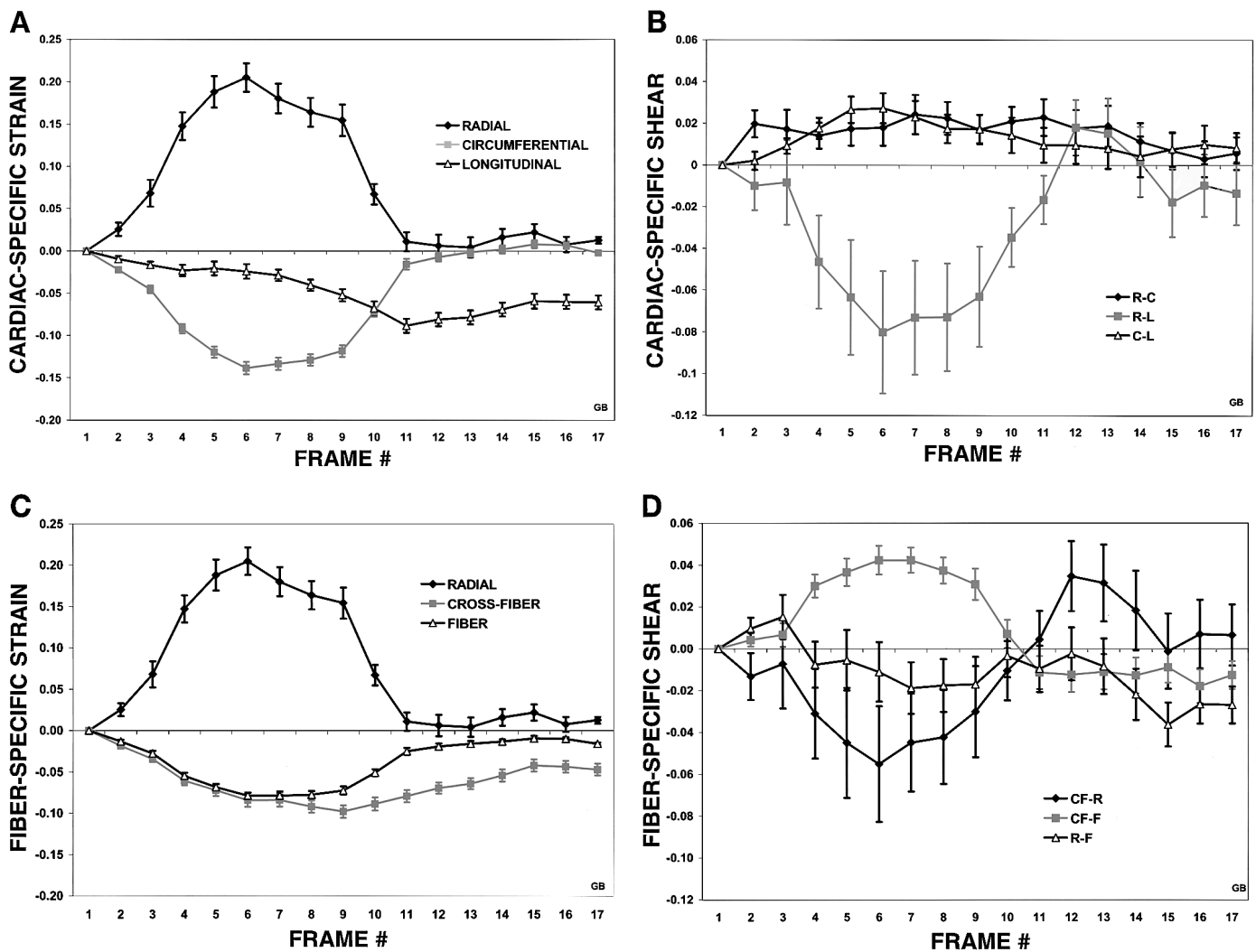


Fig. 7. Example of temporal changes in average cardiac- and fiber-specific strains and shears over the entire cardiac cycle from a representative dog. Average strains (\pm SE) are shown at each of the 16 frames in the cardiac cycle. The first image was duplicated as *frame 17* to verify return of calculated strain to baseline. The strains (A and C) and shears (B and D) generally returned to baseline with an appropriate leveling off in late diastole. The failure of average longitudinal strains to return to baseline during diastole reflects regional variation in L strain, particularly in basal segments.

approach are generally concordant with the results reported by the use of invasive measures. However, we were able to define spatial heterogeneity in these cardiac-specific indices of deformation. We observed a large apex-to-base gradient in the longitudinal strain and radial-longitudinal (transverse) shear. A similar gradient in longitudinal strain has been recently identified in human subjects with the use of color-coded pulsed-wave tissue Doppler (16). Regional differences in longitudinal tissue velocities in the endocardium have also been reported in dogs with the use of tissue Doppler (18). The observed regional variability in strains and shears may explain some of the discordant observations in the literature.

One potential limitation of this type of regional analysis with implanted markers relates to their application under conditions of regional ischemia. Observed

changes in the central ischemic region may be counterbalanced by unmeasured complex changes in the peri-ischemic border or remote regions. Thus important changes in the spatial patterns of deformation associated with regional ischemia cannot be adequately evaluated by using the implanted bead approach. The potential effects of the altered shape of the ischemic region also cannot be assessed with a transmural array of beads. These studies highlight the necessity for methods, which can provide a comprehensive 3-D measurement of myocardial deformation.

Comprehensive Image-Based Analysis of 3-D Deformation

Several imaging approaches for the temporal analysis of true 3-D cardiac deformation have also been

pursued. The MR imaging techniques include radial tagging, specific spatial modulation of magnetization, and phase-contrast imaging. MR tagging of the myocardium is one of the most popular approaches to track motion (3, 45). The advent of MR myocardial tagging techniques enabled the visualization of myocardial deformations associated with contraction at rest and after an ischemic insult. MR tagging involves creation of signal voids in the tomographic data, which deform with the myocardium, permitting the nontraumatic measurement of regional deformation. Whereas initial approaches for MR tagging provided 2-D information, recent approaches have permitted analysis of true 3-D deformations (4–6). Azhari et al. (4) evaluated several MR image-derived 3-D strain parameters for discrimination of ischemic and nonischemic regions. Three-dimensional myocardial deformations were computed for 24 myocardial segments and related to regional microsphere flow and postmortem histochemical staining. However, analysis of regional function did not correlate well with the level of ischemia, highlighting a potential limitation of this well-accepted MR tagging approach.

Bogaert and Rademakers (6) recently employed the MR tagging approach to define the normal patterns of 3-D deformation in the adult human left ventricle. In this large clinical study, both cardiac- and fiber-specific strains were generated. These investigators demonstrated a regional nonuniformity of left ventricular strains, which was similar to our findings that used a comprehensive nontagging approach. However, their analysis was limited by lower image resolution. In addition, their strain calculations were restricted to analysis of a sparse set of nodal points defined by the intersections of the tagging stripes with the endocardial and epicardial surface of the heart.

The tagging approach has the following limitations: 1) MR tags are difficult to detect throughout the cardiac cycle as tags tend to decay due to T_1 relaxation, 2) tags are not easily extended to tracking points from 3-D image sequences, and 3) for regional wall motion analysis, additional methods are required for identifying the precise tag locations and defining myocardial boundaries.

As an alternative to MR tagging, several investigators have analyzed changes in phase due to motion of tissue within a fixed volume of interest to estimate instantaneous, localized velocities, and ultimately cardiac deformation (1, 28, 34, 41). This technique identifies the change in MR signal phase (which is proportional to velocity) associated with uniform motion of tissue in the presence of a magnetic field gradient.

These widely employed MR approaches for assessment of myocardial deformation assume that the MR images provide absolute uncorrupted information regarding myocardial strains, ignoring potential errors associated with image acquisition, image processing, or through-plane motion. In our comprehensive 3-D shape-based approach for quantification of regional myocardial deformation, we impart a biomechanical

model in the analysis of the image data to help constrain the image-derived displacements, by reducing the errors associated with imaging. Our biomechanical model is based on previously derived information of myocardial mechanics obtained with the use of highly invasive measures. The use of prior knowledge in combination with a comprehensive 3-D image set strengthens our more physiological approach. In the future, we may be able to improve our biomechanical model as additional information becomes available.

In the current study, the shape of the endocardial and epicardial surfaces was used to track the 3-D trajectories of a dense field of points approach follows the complex regional deformation of the myocardium, guided by shape-matched displacements found at the bounding surfaces of the myocardium (13, 25, 38, 39). The shape-based surface displacements are integrated with a continuum biomechanics model incorporating myofiber architecture to estimate fiber-specific endocardial and epicardial strains and shears (32). This shape-based approach has the advantage of being able to track deformation over the entire cardiac cycle, and would be applicable to any high-resolution 3-D imaging modality, which defines the myocardial surfaces over the entire cardiac cycle.

Calculation of Fiber-Specific Strains and Shears

The fiber-specific strains and shears derived in this study correlate with findings derived with the use of biplane cine radiography of implanted beads or implanted sonomicrometers. Rodriguez et al. (36), employing implanted sonomicrometers in combination with careful histological analysis, demonstrated that fiber-specific strains were fairly uniform across the wall (epicardial, -0.14 ; midwall, -0.14 ; and endocardial, -0.12) and similar in magnitude to our estimated fiber strains. Waldman et al. (44), employing biplane

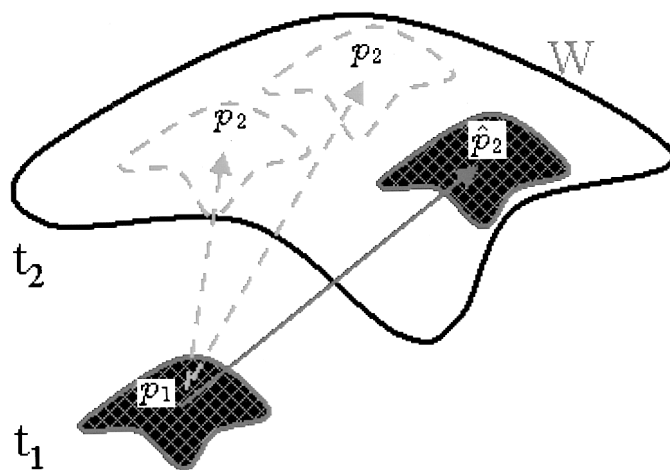


Fig. 8. Example of shape-tracking approach. The original surface is mapped to the final surface. For point p_1 on the original surface, a window region (W) of plausible matching points on the final surface is first generated. Point p_2 in W , which has the most similar shape properties to p_1 , is then selected as the candidate match point. t , Time.

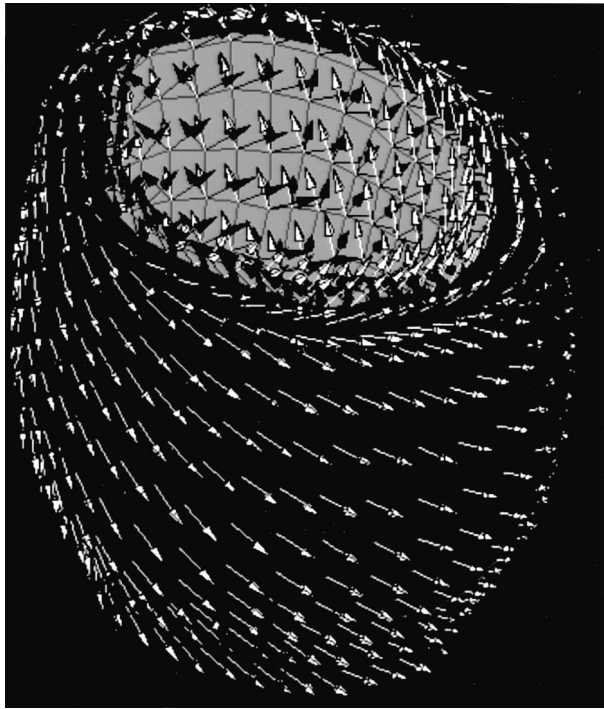


Fig. 9. Map of fiber direction in the left ventricle.

cine radiography of implanted beads, demonstrated epicardial (-0.09 ± 0.04) and endocardial (-0.06 ± 0.06) fiber strains nearly identical to those observed by using our shape-based analysis. LeGrice et al. (22) observed regional differences in longitudinal-radial (transverse) shear using biplane cine radiography of implanted beads placed in the septum and anterior free wall. These investigators reported positive transverse shear in the endocardium of the anterior left ventricular wall and negative shears in the septum. The differences in shear were attributed to regional differences in myocardial cleavage planes in these two regions. The approach employed by these investigators limits the analysis to very small regions of the left ventricle. Our findings suggest that there are significant regional differences in longitudinal-radial shear from apex to base, as well as around the circumference of the left ventricle. This would indicate that the apex to base location of the implanted beads could tremendously alter the observations. Thus there appears to be significant regional variation between regional wall thickening (radial strain) and longitudinal-radial shear. In our analysis, there was a weak direct linear

relationship between regional transmural radial strain and longitudinal-radial shear ($r = 0.43$, $P = 0.03$).

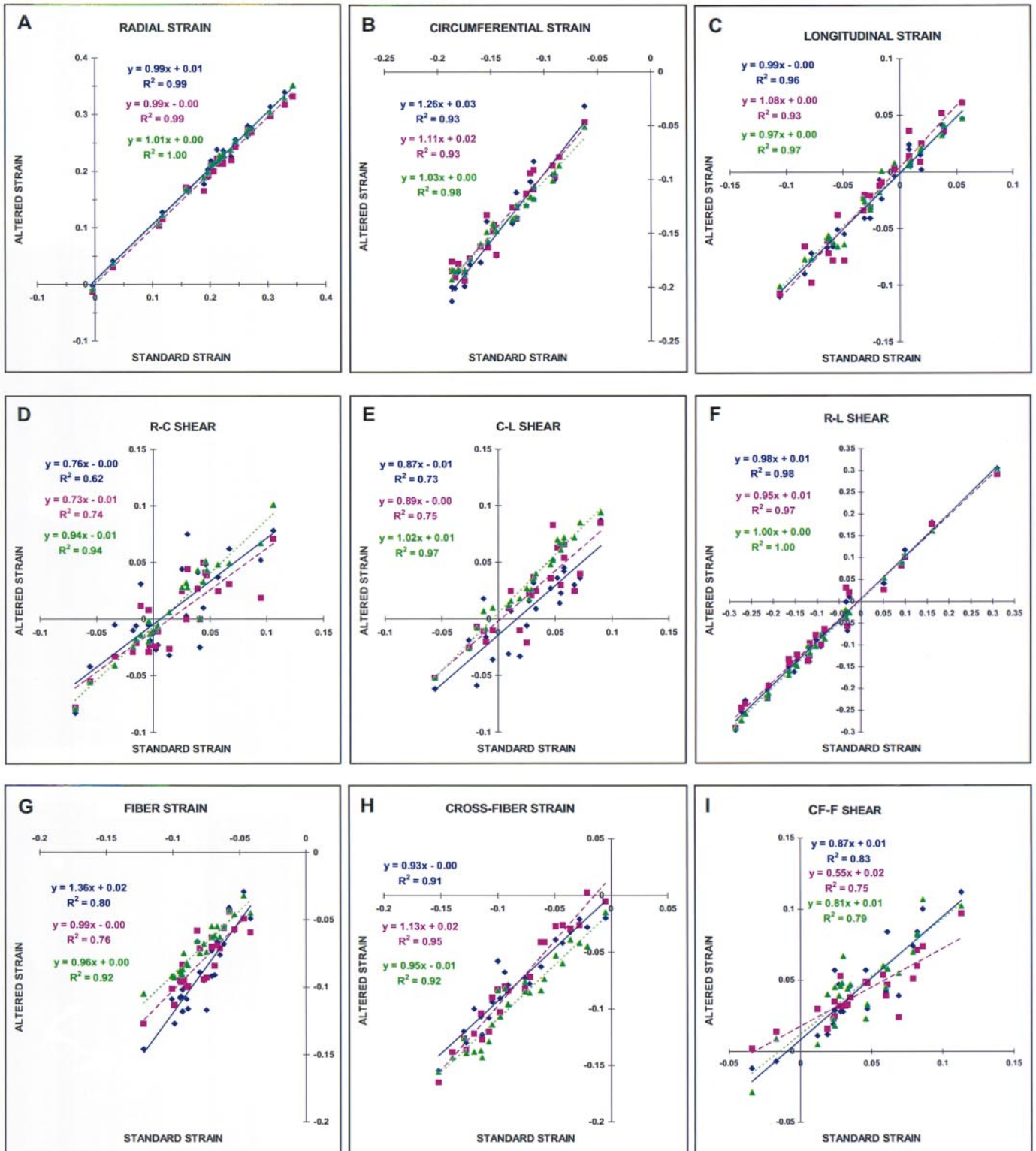
Limitations

Our analysis of regional myocardial deformation was limited to normal resting conditions. In our analysis of fiber-specific strains, we assume uniform fiber architecture as previously established in the literature. This standard fiber architecture may not be applicable following myocardial infarction or in the presence of diseased states like asymmetric septal hypertrophy, which would distort the fiber architecture. In the future, we may be able to noninvasively derive information regarding the fiber architecture by using MR diffusion imaging (17, 35). These additional MR imaging sequences may need to be incorporated in future applications of our strain computations.

Our model may also force endocardial-to-epicardial gradients in strain, based on assumptions regarding conservation of volume. This bias could be minimized in the future by incorporating midwall information, derived by using either MR tagging or phase-velocity mapping. We have primarily focused our analysis to the systolic portion of the cardiac cycle. Analysis of regional myocardial strains in the diastolic phase of the cardiac cycle was complicated by image flow artifacts in some of the dogs. Analysis of diastole was also limited by the time required for segmentation of the entire cardiac cycle. However, our approach could be extended to analysis of the entire cardiac cycle, particularly if the segmentation algorithms could be further automated. An illustration of the typical changes in regional myocardial deformation over the entire cardiac cycle is provided in Fig. 7, A–D.

Our methods remain sensitive to variations in image quality and resolution and are primarily limited by accurate and efficient segmentation of the left ventricular surface. In our current 3-D algorithms, we have not incorporated a potentially important constraint in the analysis, which would require periodicity (i.e., a return of the final coordinate position back to the point of origin). We have found this constraint useful in our previous 2-D algorithms for improving image segmentation and strain analysis. In the current analysis, resolution was also somewhat limited along the longitudinal axis due to the 5-mm MR short-axis slice thickness. This would inherently increase the error associated with calculation of longitudinal strain. The acquisition of overlapping short-axis images would improve through plane resolution and minimize this lim-

Fig. 10. Illustration of the effects of alteration in parameters of the biomechanical model on calculated cardiac-specific (A–F) and fiber-specific (G–I) ES strains in one of the dogs. Shown are scatter plots of the calculated strains and shears after alteration of model parameters (y-axis) relative to values derived using our standard model (x-axis). Segment-for-segment differences are shown when assuming an isotropic model (no differential fiber stiffness). The equations for these correlations are shown in blue. Also illustrated are the effects of changing the Poisson's ratio to 0.3 to model the myocardium as more compressible. The equations for these correlations are shown in pink. The slopes for these correlations were close to unity. Finally, strains were calculated assuming a slightly rotated fiber architecture. The effects of altering the fiber architecture are shown in green. The effects of all of these changes were relatively small for our calculated transmural strains.



GB

itation. Preliminary studies using this overlapping approach confirm the current observations regarding the normal gradients in longitudinal strain.

We have also ignored respiratory motion in our acquisition of the MR short-axis MR images. Respiratory motions are averaged over the course of acquiring the full 3-D data set. With the advancement of MR imaging hardware and software these motions could also be eliminated. Correction for respiratory motion will likely improve the analysis by using our shape-tracked approach.

Clinical Implications

To date, quantitative noninvasive assessment of regional myocardial strain from 3-D images has been limited to specific MR acquisitions, in particular, MR tagging or MR phase-contrast velocity analysis. Our shape-based approach, which employs finite element analysis and a biomechanical model-based strategy, provides a comprehensive analysis of regional 3-D myocardial deformation. This surface-based approach would be applicable to standard cine-gradient MR images, 3-D cine computed tomographic images, and 3-D echocardiography. However, widespread application of our shape-based approach will require improved image segmentation. The application of our approach to 3-D echocardiography may be facilitated by the use of echocardiographic contrast agents and would potentially bring accurate quantitative analysis of regional myocardial deformation to the patient's bedside.

APPENDIX

Description of Strain Estimation Algorithm

Shape-tracking displacement estimates. In this study, the original displacements on the inner and outer surfaces of the left ventricular myocardium were obtained by using the shape-tracking algorithm previously described in detail (39). This approach is outlined below.

An illustration of this process is provided by Fig. 8. Consider point p_1 on a surface at time t_1 , which is to be mapped to a point p_2 on the deformed surface at time t_2 . First, a search is performed on a physically plausible region W on the deformed surface and the point p_2 , which has the local shape properties closest to those p_1 is selected. The shape properties here are captured in terms of the principal curvatures κ_1 and κ_2 . The distance measure used is the bending energy required to bend a curved plate or surface patch to a newly deformed state. This is labeled as d_{be} and is defined as

$$d_{be}(p_1, p_2) = \left\{ \frac{[\kappa_1(p_1) - \kappa_1(p_2)]^2 + [\kappa_2(p_1) - \kappa_2(p_2)]^2}{2} \right\} \quad (A1)$$

The displacement estimate vector for each point p_1 , μ_1^m , is given by

$$\mu_1^m = \tilde{p}_2 - p_1, \quad \tilde{p}_2 = \arg \min_{p_2 \in W_2} [d_{be}(p_1, p_2)] \quad (A2)$$

Confidence measures in the match. Bending energy measures for all the points inside the search region W are recorded as the basis to measure the "goodness and uniqueness" of the matching choices. The confidence is high if the best match is both good and unique and falls off otherwise.

Modeling the Myocardium

The passive properties of the left ventricular myocardium are captured using a biomechanical model. We use a transversely isotropic linear elastic model, which allows us to incorporate information about the preferential stiffness of the tissue along fiber directions as previously defined (19). These fiber directions are shown in Fig. 9. The model described in terms of an internal or strain energy function of the form

$$W = \epsilon' \mathbf{C} \epsilon \quad (A3)$$

where ϵ is the strain and \mathbf{C} is the 6×6 matrix containing the elastic constants, which define the material properties.

$$\mathbf{C}^{-1} = \begin{bmatrix} \frac{1}{E_p} & -\frac{\nu_p}{E_p} & -\frac{\nu_{fp}}{E_f} & 0 & 0 & 0 \\ -\frac{\nu_p}{E_p} & \frac{1}{E_p} & -\frac{\nu_{fp}}{E_f} & 0 & 0 & 0 \\ -\frac{\nu_{fp}}{E_f} & -\frac{\nu_{fp}}{E_f} & \frac{1}{E_f} & 0 & 0 & 0 \\ 0 & 0 & 0 & \frac{2(1+\nu_p)}{E_p} & 0 & 0 \\ 0 & 0 & 0 & 0 & \frac{1}{G_f} & 0 \\ 0 & 0 & 0 & 0 & 0 & \frac{1}{G_f} \end{bmatrix} \quad (A4)$$

where E_f is the fiber stiffness, E_p is cross-fiber stiffness, ν_f and ν_p are the corresponding Poisson's ratios, and G_f is the shear modulus across fibers [$G_f \approx E_f/2(1 + \nu_{fp})$]. If $E_f = E_p$ and $\nu_{fp} = \nu_p$, this model reduces to the more common isotropic linear elastic model. The fiber stiffness was set to be 3.5 times greater than the cross-fiber stiffness (19). The Poisson's ratios were both set to 0.4 to model approximate incompressibility. More details can be found in a continuum mechanics textbook (23).

To evaluate the potential significance of these assumptions regarding the fiber architecture, differential fiber stiffness, and index of incompressibility, we computed end-systolic cardiac- and fiber-specific strains and shears in one of the dogs by using different model parameters. These differences are illustrated in Fig. 10. We first calculated the strains with and without the fiber architecture in our mechanical model. The mechanical model became isotropic without the differential fiber stiffness. We then computed strains with a 10° rotation in the assumed fiber axes. Finally, we computed strains by using a lower Poisson's ratio of 0.3, modeling the tissue as more compressible. The effects of these changes were relatively small for our calculated transmural strains. Changing the fiber angle produced predictable changes in the fiber and cross-fiber strains. Slightly greater effects were seen for the calculated shears. On the basis of these additional analyses, our mechanical model does not appear overly sensitive to small changes in the model parameters or assumed fiber architecture. However, these differences might be greater for the calculated strains and shears in each of the smaller midwall elements in our finite element analysis because calculation of the strains within the myocardium would be more dependent on the mechanical model and fiber architecture.

Integrating the Data and Model Terms

Having defined both the data term model and the model term, we discretize the equations by using the finite element method to generate the final equation, which takes the form

$$\mathbf{KU} = \mathbf{A}(\mathbf{U}^e - \mathbf{U}) \quad (\text{A5})$$

This equation is solved to find the displacement field \mathbf{U} , which can then be differentiated to compute strain.

We gratefully acknowledge the technical assistance of Dr. Cindy Shi, Dr. Jennifer Hu, Dr. Eliot N. Heller, Dr. Edouard Daher, Dr. Michael Shen, Michael Singer, Peter Borek, Jason Soares, and Donna Dione. We also thank Lawrence Staib for invaluable suggestions and guidance.

REFERENCES

1. Arai A, Gaither C, Epstein F, Balaban R, and Wolff S. Myocardial velocity gradient imaging by phase contrast MRI with application to regional function in myocardial ischemia. *Magn Reson Med* 42: 98–109, 1999.
2. Axel L and Dougherty L. MR imaging of motion with spatial modulation of magnetization. *Radiology* 171: 841–845, 1989.
3. Axel L, Goncalves R, and Bloomgarden D. Regional heart wall motion: two-dimensional analysis and functional imaging with MR imaging. *Radiology* 183: 745–750, 1992.
4. Azhari H, Weiss J, Rogers W, Siu C, and Shapiro E. A noninvasive comparative study of myocardial strains in ischemic canine hearts using tagged MRI in 3-D. *Am J Physiol Heart Circ Physiol* 268: H1918–H1926, 1995.
5. Azhari H, Weiss J, Rogers W, Siu C, Zerhouni E, and Shapiro E. Noninvasive quantification of principal strains in normal canine hearts using tagged MRI images in 3-D. *Am J Physiol Heart Circ Physiol* 264: H205–H216, 1993.
6. Bogaert J and Rademakers F. Regional nonuniformity of normal adult human left ventricle. *Am J Physiol Heart Circ Physiol* 280: H610–H620, 2001.
7. Chakraborty A, Staib L, and Duncan J. An integrated approach to boundary finding. *IEEE Workshop on Biomedical Image Analysis, Seattle, WA, 1994*, p. 13–22.
8. Chakraborty A, Worring M, and Duncan J. On multi-feature integration for deformable boundary finding. *International Conference on Computer Vision, 1995*, p. 846–851.
9. Costa KD, Takayama Y, McCulloch AD, and Covell JW. Laminar fiber architecture and three-dimensional systolic mechanics in canine ventricular myocardium. *Am J Physiol Heart Circ Physiol* 276: H595–H607, 1999.
10. Dione D, Shi P, Smith W, DeMan P, Soares J, Duncan J, and Sinusas A. Three-dimensional regional left ventricular deformation from digital sonomicrometry. *Proc 19th Annu Int Conf IEEE Eng Med and Biol Soc, 1997*, p. 848–851.
11. Duncan J, Lee F, Smeulders A, and Zaret B. A bending energy model for measurement of cardiac shape deformity. *IEEE Trans Med Imaging* 10: 307–320, 1991.
12. Duncan J, Shi P, Constable R, and Sinusas A. Physical and geometrical modeling of image-based recovery of left ventricular deformation. *Prog Biophys Mol Biol* 69: 333–351, 1998.
13. Duncan J, Shi PC, Amini A, Constable R, Staib L, Dione D, Shi QX, Heller E, Singer M, Chakraborty A, Robinson G, Gore J, and Sinusas A. Towards reliable noninvasive measurement of myocardial function from 4D images. *SPIE Proc Medical Imaging*. Newport Beach, CA: 1994.
14. Fenton T, Cherry J, and Klassen G. Transmural myocardial deformation in the canine left ventricular wall. *Am J Physiol Heart Circ Physiol* 235: H523–H530, 1978.
15. Freeman GL, LeWinter MM, Engler RL, and Covell JW. Relationship between myocardial fiber direction and segment shortening in the midwall of the canine left ventricle. *Circ Res* 56: 31–39, 1985.
16. Galiuto L, Ignone G, and DeMaria A. Contraction and relaxation velocities of the normal left ventricle using pulsed-wave tissue Doppler echocardiography. *Am J Cardiol* 81: 609–614, 1998.
17. Garido L, Wedeen V, Kwong K, Spencer U, and Kantor H. Anisotropy of water diffusion in the myocardium of the rat. *Circ Res* 74: 789–793, 1994.
18. Gorscan J, Strum D, Mandarino W, Gulati V, and Pinsky M. Quantitative assessment of alterations in regional left ventricular contractility with color-coded tissue Doppler echocardiography: comparison with sonomicrometry and pressure-volume relations. *Circulation* 95: 2423–2433, 1997.
19. Guccione J and McCulloch A. Finite element modeling of ventricular mechanics. In: *Theory of Heart*, edited by Hunter P, McCulloch A, and Nielsen P. Berlin: Springer-Verlag, 1991, p. 122–144.
20. Holman E, Buller V, deRoos A, van der Geest R, Baur L, van der Laarse A, Bruschke A, Reiber J, and van der Wall E. Detection and quantification of dysfunctional myocardium by magnetic resonance imaging: a new three-dimensional method for quantitative wall-thickening analysis. *Circulation* 95: 924–931, 1997.
21. Huebner K, Thornton E, and Byrom T. *The Finite Element Method For Engineers*. New York: Wiley, 1995.
22. LeGrice IJ, Takayama Y, and Covell JW. Transverse shear along myocardial cleavage planes provides a mechanism for normal systolic wall thickening. *Circ Res* 77: 182–193, 1995.
23. Malvern L. *Introduction to the Mechanics of a Continuous Medium*. Englewood Cliffs, NJ: Prentice Hall, 1969.
24. McCulloch AD and Omens JH. Non-homogeneous analysis of three-dimensional transmural finite deformation in canine ventricular myocardium. *J Biomech* 24: 539–548, 1991.
25. McEachen J and Duncan J. Shape-based tracking of naturally occurring annuli in image sequences. *IEEE Conf Computer Vision and Pattern Recognition, 1993*.
26. McEachen J and Duncan J. Shaped-based tracking of left ventricular wall motion. *IEEE Trans Med Imaging* 16: 270–283, 1997.
27. Meoli D, Mazhari R, Dione D, Omens J, McCulloch A, and Sinusas A. Three dimensional digital sonomicrometry: comparison with biplane radiography. *IEEE 24th Annual NE Bioeng Conf, 1998*, p. 64–67.
28. Nayler G, Firmin D, and Longmore D. Blood flow imaging by CINE magnetic resonance. *J Comput Assist Tomogr* 10: 715–722, 1986.
29. Ono S, Waldman L, Yamashita H, Covell J, and Ross J. Effect of coronary reperfusion on transmural myocardial remodeling in dogs. *Circulation* 91: 1143–1153, 1995.
30. Papademetris X. Estimation of 3D left ventricular deformation from medical images using biomechanical models. (PhD Thesis). New Haven, CT: Yale University, 2000.
31. Papademetris X, Rambo J, Dione D, Sinusas A, and Duncan J. Visually interactive semi-automated 3D segmentation of cine cardiac magnetic resonance images (Abstract). *J Am Coll Cardiol* 31: 7A, 1998.
32. Papademetris X, Shi P, Dione D, Sinusas A, Constable R, and Duncan J. Recovery of soft tissue object deformation from 3D image sequences using biomechanical models. In: *Information Processing in Medical Imaging*. Visegrad, Hungary: Springer Lecture Notes in Computer Science, 1999, p. 352–356.
33. Papademetris X, Sinusas A, Dione D, and Duncan J. Estimation of 3D left ventricular deformation from echocardiography. *Med Image Anal* 5: 17–28, 2001.
34. Pelc N, Bernstein M, Shimakawa A, and Glover G. Encoding strategies for three direction phase contrast MR imaging of flow. *J Magn Reson Imaging* 1: 405–413, 1991.
35. Reese TG, Weisskoff RM, Smith RN, Rosen BR, Dinsmore RE, and Wedeen VJ. Imaging myocardial fiber architecture in vivo with magnetic resonance. *Magn Reson Med* 34: 786–791, 1995.
36. Rodriguez E, Hunter W, Royce M, Leppo M, Douglas A, and Weisman H. A method to reconstruct myocardial sarcomere lengths and orientation at transmural sites in beating canine hearts. *Am J Physiol Heart Circ Physiol* 263: H293–H306, 1992.

37. Sheehan FH, Bolson EL, Dodge HT, Mathey DG, Schofer J, and Woo HW. Advantages and applications of the centerline method for characterizing regional ventricular function. *Circulation* 74: 293–305, 1986.
38. Shi P, Sinusas A, Constable R, and Duncan J. Volumetric deformation analysis using mechanics-based data fusion: applications in cardiac motion recovery. *Int J Computer Vision* 35: 87–107, 1999.
39. Shi P, Sinusas AJ, Constable RT, Ritman E, and Duncan JS. Point-tracked quantitative analysis of left ventricular surface motion from 3-D image sequences. *IEEE Trans Med Imaging* 19: 36–50, 2000.
40. Streeter DJ, Spotnitz H, Patel D, Ross JJ, and Sonnenblick E. Fiber orientation in the canine left ventricle during diastole and systole. *Circ Res* 24: 339–347, 1969.
41. Van Dijk P. Direct cardiac NMR imaging of heart wall and blood flow velocity. *J Comput Assist Tomogr* 8: 429–436, 1984.
42. Villarreal F, Lew W, Waldman L, and Covell J. Transmural myocardial deformation in the ischemic canine left ventricle. *Circ Res* 68: 368–381, 1991.
43. Waldman L, Fung Y, and Covell J. Transmural myocardial deformation in the canine left ventricle: normal in vivo three-dimensional finite strains. *Circ Res* 57: 152–163, 1985.
44. Waldman LK, Nosan D, Villarreal F, and Covell JW. Relation between transmural deformation and local myofiber direction in canine left ventricle. *Circ Res* 63: 550–562, 1988.
45. Zerhouni E, Parish D, Rogers W, Yang A, and Shapiro E. Human heart: tagging with MR imaging—a method for noninvasive assessment of myocardial motion. *Radiology* 169: 59–63, 1988.

